

PAPER

[View Article Online](#)
[View Journal](#) | [View Issue](#)Cite this: *J. Mater. Chem. A*, 2023, **11**, 232Boosting the efficiency of urea synthesis via cooperative electroreduction of N₂ and CO₂ on MoP†Dongxu Jiao,^{‡ab} Yilong Dong,^{‡b} Xiaoqiang Cui,^{id}*^b Qinghai Cai,^{id}*^{ac}
Carlos R. Cabrera,^d Jingxiang Zhao^{id}*^a and Zhongfang Chen^{id}*^e

By combining theoretical and experimental efforts, we designed the MoP-(101) surface and explored its potential as catalyst for urea production. Our computations revealed that N₂ and CO₂ reactants can be effectively reduced to urea on the MoP-(101) surface with a low limiting potential (−0.27 V); the competitive side reactions are well suppressed, and the *NHCONH species is a key reaction intermediate for the C–N coupling during urea synthesis. Our experimental measurements confirmed the above theoretical predictions: urea synthesis was achieved with the urea formation rate of 12.4 μg h^{−1} mg^{−1} and the faradaic efficiency of 36.5%. This work not only highlights the critical role of the abundant Mo active sites for urea electrosynthesis but also provides a new mechanism for C–N coupling, which may be used to further develop other efficient electrocatalysts.

Received 26th September 2022
Accepted 16th November 2022

DOI: 10.1039/d2ta07531h

rsc.li/materials-a

1. Introduction

As one of the most important nitrogen fertilizers, urea has fed about 19% of the world's population over the past century due to its high nitrogen content.^{1–3} Furthermore, urea is a critical feedstock to manufacture fine chemicals, such as urea-formaldehyde, ureamelamine-formaldehyde resins, and barbiturates.^{4,5} In addition, urea can be utilized as a promising energy carrier for sustainable hydrogen production.^{6,7} Thus, developing the urea industry is of great significance, especially for the continuously growing human population and for its extensive applications in energy storage and conversion.

To date, industrial-scale urea production mainly comes from the reaction of NH₃ with CO₂.^{8,9} Note that the Haber–Bosch process still dominates NH₃ synthesis from the industrial fixation of N₂ and H₂,^{10–12} of which about 80% is consumed for urea

generation.¹³ The Haber–Bosch process requires harsh conditions (400–650 °C and 200–400 bar) due to the inert N≡N triple bonds; it is responsible for 1–2% of world's energy consumption and *ca.* 1.4% of CO₂ emissions.^{14,15} In this scenario, the exploration of a sustainable, efficient, and environmentally benign route enabling N₂ and CO₂ to directly convert into urea at ambient conditions is highly desirable.¹⁶ In this regard, electrocatalysis holds great promise for urea synthesis, as it can effectively convert renewable energy and feedstock into high-value-added chemicals under mild conditions.¹⁷

Very recently, the simultaneous electrocatalytic activation of N₂ and CO₂ to generate urea by their C–N coupling has emerged as an attractive alternative strategy to the energy-intensive industrial process.¹⁸ Nevertheless, electrocatalytic urea production generally suffers from extremely low activity and selectivity due to the following substantial challenges: (1) weak adsorption of inert N₂ and CO₂ reactants; (2) difficulty in dissociating N≡N and C=O bonds; (3) the kinetically sluggish C–N coupling.¹⁹ Therefore, these challenges have to be overcome when developing highly efficient catalysts for urea production. Encouragingly, some promising catalysts have been recently developed.^{19–22} For example, Wang's group successfully realized urea electrosynthesis on a PdCu alloyed nanoparticle by the coupling of N₂ and CO₂ in H₂O under ambient conditions;²⁰ Yuan *et al.* successfully fabricated BiFeO₃/BiVO₄,⁹ InOOH,¹⁹ Ni₃(BO₃)₂,²¹ and Bi–BiVO₄ (ref. 22) to boost the formation of urea. However, there is still a lack of highly efficient and selective electrocatalysts with specific and abundant active sites that can simultaneously capture and activate N₂ and CO₂ to form urea, and developing such catalysts is highly rewarding but remains a huge challenge.

^aCollege of Chemistry and Chemical Engineering, Key Laboratory of Photonic and Electronic Bandgap Materials, Ministry of Education, Harbin Normal University, Harbin 150025, China. E-mail: xjz_hmily@163.com

^bState Key Laboratory of Automotive Simulation and Control, School of Materials Science and Engineering, Key Laboratory of Automobile Materials of MOE, Jilin University, Changchun 130012, China. E-mail: xqcui@jlu.edu.cn

^cHeilongjiang Province Collaborative Innovation Center of Cold Region Ecological Safety, Harbin 150025, China

^dDepartment of Chemistry and Biochemistry, The University of Texas at El Paso, El Paso, Texas 79968, USA

^eDepartment of Chemistry, University of Puerto Rico, Rio Piedras Campus, San Juan, Puerto Rico 00931, USA. E-mail: zhongfangchen@gmail.com

† Electronic supplementary information (ESI) available. See DOI: <https://doi.org/10.1039/d2ta07531h>

‡ Dongxu Jiao and Yilong Dong contributed equally to this work.

Due to its various oxidation states from -2 to $+4$, molybdenum (Mo) possesses rich and intriguing chemistry,^{23–25} and Mo-based materials have emerged as promising electrocatalysts in many energy conversion reactions, especially for nitrogen reduction reaction (NRR) and CO_2 reduction reaction (CO_2RR).^{26–31} For example, Jiang and coworkers reported that MoB_2 exhibits excellent NRR performance with a high faradaic efficiency of 30.84%,³¹ while Wu *et al.* fabricated a peculiar sub-monolayer MoS_{2-x} structure that was revealed to display superior electrocatalytic NRR performance at ultralow overpotential (-0.2 V. *vs.* RHE).²⁹ In addition, Sun *et al.* reported that MoP nanoparticles supported on In-doped porous carbon have outstanding performance for CO_2 reduction to formate, with a high faradaic efficiency (96.5%) and excellent current density (43.8 mA cm^{-2}).³⁰

Among various Mo-based materials, molybdenum phosphide (Mo_xP_y) materials have been actively investigated as non-precious-metal catalysts in electrocatalysis due to their unique physicochemical properties, such as high chemical stability, excellent conductivity, and earth-abundant reserves.^{31,32} In particular, as the electronegativity of P (2.1) is slightly larger than that of Mo (1.8), the incorporation of P will induce a small electron transfer from Mo to P, leading to a moderate coupling between Mo-d and P-p orbitals. As a result, the d-band center of Mo_xP_y may move down as compared with the pure Mo metals, leading to an optimal binding strength with adsorbates.³³ Furthermore, the positively charged Mo atoms may sufficiently boost the N_2 and CO_2 activation. In addition, when the electron-deficient Mo layer in Mo_xP_y materials is exposed, abundant Mo active sites become available, which may be beneficial to the simultaneous activation of inert N_2 and CO_2 reactants in urea synthesis. Therefore, it is very likely that Mo_xP_y materials with exposed Mo surface can achieve the goal of highly efficient urea synthesis at ambient conditions.

Herein, by means of density functional theory (DFT) computations, we explored the catalytic activity of MoP material for urea synthesis. As expected, the Mo-terminated (101) surface, which is energetically the most favorable surface of MoP material, can simultaneously bind N_2 and CO_2 strongly, with the free energy change of -0.70 eV. Interestingly, the adsorbed N_2 and CO_2 can be further reduced into urea product with a rather low limiting potential of -0.27 V. Remarkably, our theoretical predictions were verified by our proof-of-concept experiments: the as-synthesized MoP material exhibits good catalytic activity with a urea yield of $12.4 \mu\text{g h}^{-1} \text{ mg}^{-1}$ and selectivity, with a faradaic efficiency of 36.5% (-0.35 V *vs.* RHE) for urea synthesis.

2. Experimental section

2.1. Computational detail

All spin-polarized density functional theory (DFT) computations were performed using a plane-wave basis set, as implemented within the Vienna *Ab Initio* Simulation Package (VASP).^{34,35} The projector augmented wave (PAW) potential was employed to describe the interactions between electrons and ions.^{36,37} The exchange–correlation interactions were determined by the

Perdew–Burke–Ernzerhof (PBE) functional within the generalized gradient approximation (GGA).³⁸ The empirical correction in Grimme's method (DFT + D3) was used to describe the van der Waals (vdW) interactions,³⁹ and the climbing image nudged elastic band (CI-NEB) method was utilized to locate the involved transition states.⁴⁰ A cutoff energy of 550 eV was adopted for the plane-wave basis set, and the convergence criterion for the residual force and the energy on each atom during structural analysis were set to 0.01 eV \AA^{-1} and 10^{-5} eV, respectively.

The (100), (001) and (101) surfaces of MoP with different terminations were considered to evaluate the stability and catalytic activity for urea synthesis. These surface models were built by cleaving the bulk MoP structure, and a 3×3 supercell was adopted for these surfaces. All these models consist of four atomic layers; the bottom two atomic layers were fixed, while the upper two layers were fully relaxed during geometry optimizations. The vacuum space was set to be 20 Å in the *z*-direction to avoid the interactions between periodic images. A $3 \times 3 \times 1$ Monkhorst–Pack *k*-point mesh was adopted to sample the Brillouin zone.

To assess the thermodynamic stability of different MoP surfaces, the surface energy (γ) was determined by $\gamma = \frac{1}{2A}(E_{\text{slab}}^{\text{relax}} - N_{\text{atoms}} \times E_{\text{bulk}})$, where *A* is the surface area, $E_{\text{slab}}^{\text{relax}}$ denotes the energy of the relaxed slab, N_{atoms} is the number of atoms in the slab, and E_{bulk} is the bulk energy per atom. According to this definition, a smaller γ suggests a better thermodynamic stability.

The computational hydrogen electrode (CHE) model^{41,42} was used to compute the change in the Gibbs free energy (ΔG) of each elementary step during urea electrosynthesis, in which one-half of the chemical potential of hydrogen molecule is equal to the chemical potential of the proton–electron pair. In this CHE model, the ΔG value of each elementary step can be obtained by $\Delta G = \Delta E + \Delta E_{\text{ZPE}} - T\Delta S + \Delta G_U$, where ΔE represents the reaction energy difference of reactant and product, which can be directly computed from DFT computations. ΔE_{ZPE} and ΔS are the changes in zero-point energies and entropy at room temperature ($T = 298.15$ K), which can be computed from the vibrational frequencies. The entropies of the free molecules, such as N_2 , CO_2 , and H_2 , were taken from the NIST database. $\Delta G_U = -eU$, where *e* is the transferred charge and *U* represents the applied potential at the electrode. The limiting potential (U_L) was employed to assess the catalytic activity for urea formation, which can be computed by: $U_L = -\max(\Delta G_1, \Delta G_2, \Delta G_3, \Delta G_4, \dots, \Delta G_i)/e$, where ΔG_i represents the free energy change of each elementary step in the whole electrochemical process. According to this definition, a less negative U_L on a given catalyst denotes a less energy input, thus suggesting its higher catalytic activity toward urea formation.

2.2. Characterizations

The crystal structure of all samples was characterized using X-ray diffraction (XRD) with a Bragg–Brentano diffractometer (D8-tools, Germany) equipped with a Cu-K α source emitting at 0.15418 nm. The morphologies of the samples were investigated

using a field emission scanning electron microscope (FESEM) (Hitachi, SU8010, Japan). Transmission electron microscopy (TEM) and high-resolution TEM (HRTEM) were performed using a JEM-2000EX transmission electron microscope (JEOL Co., Japan). X-ray photoelectron spectroscopy (XPS) was measured using an ESCALAB-250XI instrument with Al K α X-ray radiation (Thermo Fisher Scientific, USA). UV-vis absorption spectra were recorded by the diffuse reflection method with a UV-2550 spectrometer (Shimadzu Co., Japan).

2.3. Preparation of electrode

First, 2 mg catalyst was dispersed into a mixed solution of 950 μ L ethanol and 50 μ L Nafion (5 wt% solution) with sonication for 30 minutes. Then, 100 μ L of catalyst solution was drop-casted on a piece of carbon paper and dried naturally to form a working electrode. The area of the working electrode is 1 cm², and the catalyst concentration is 0.2 mg cm⁻².

2.4. Electrochemical measurements

The electrochemical test was carried out in an H-type cell with a three-electrode system on a CHI 1140c electrochemical station (Chenhua Co., China). Pretreated Nafion117 membrane was used as diaphragm. The electrolyte solution used during the reaction was 0.1 M KHCO₃. Electrochemical tests were carried out with a Pt foil as the counter electrode and an Ag/AgCl electrode filled with saturated KCl aqueous solution as the reference electrode. Before the electrochemical test, N₂/CO₂ mixed gas was bubbled into the electrolyte in the cathode chamber for more than 30 minutes. During the reaction, the gas flow rate was kept at 30 sccm with the N₂/CO₂ volume ratio of 1 : 1. The electrolyte was magnetically stirred at 500 rpm throughout the electrochemical tests. Potentials were converted to RHE scale using the following equation: $E_{\text{RHE}} = E_{\text{Ag/AgCl}} + 0.0591 \times \text{pH} + 0.197$. The 0.1 M KHCO₃ aqueous solution with N₂ and CO₂ has a pH of 6.8, and the pH of unvented 0.1 M KHCO₃ aqueous solution is 8.3.

2.5. Calculation of urea yield and faradaic efficiency

The faradaic efficiency (FE) was defined as the ratio of the number of charges used to electrosynthesize urea to the total number of charges passing through the electrodes. The FE of electrosynthesis of urea could be calculated by following equation: $\text{FE} (\%) = (6 \times F \times C \times V) / (60.06 \times Q) \times 100$. The rate of formation of urea was calculated using the following equation: $\text{urea formation rate} = C \times V / (m \times t \times 60.06)$, in which F is Faraday constant (96 485), C is the mass concentration of urea in the electrolyte, V is the volume of electrolyte in the electrolytic cell, Q is the total charge during the reaction, t is the response time at different working potentials, and m is the mass loading of catalyst on the carbon paper.

3. Results and discussion

3.1. Geometry structure and stability of MoP

Based on our experimental results, six main exposed low-indexed crystal surfaces were considered, including (100),

(101), and (001) with either Mo- or P-terminations (Fig. 1a and S1†). To evaluate the thermodynamic stability of these six candidates, we computed their corresponding surface energies (γ). The Mo-exposed (101) slab has the smallest γ value (2.51 J m⁻², Fig. 1b), which is well consistent with our XRD tests (see Section 3.4). Thus, the (101) surface was chosen for exploring the catalytic performance of MoP in the following discussions. Notably, the outermost layer of (101) consists of the periodic hexagonal ring moieties, in which three Mo atoms alternatively bind with three P atoms with the length of 2.44 Å.

Furthermore, we examined the electronic properties of the MoP-(101) surface by computing the partial density of states (PDOSs) of Mo and P atoms. There are obvious hybridizations between the Mo-4d and P-3p orbitals (Fig. S2†), suggesting their strong chemical bonds and thus ensuring the high stability of this material. According to the Bader population analysis, there is about 0.49e charge transfer from Mo to P (Fig. 1c), making the 4d_{z²} orbital of Mo atom empty (locating above the Fermi level, Fig. 1d), while most of the other 4d orbitals are occupied (Fig. S2†). Thus, the co-existence of empty and occupied d orbitals in the surface Mo atoms makes it possible for the surface Mo atoms to accept the lone-pair electrons of N₂ and CO₂, and at the same time donate electrons into anti-bonding orbitals of N₂ and CO₂, thus leading to an “acceptance–donation” process, which could be conducive to the sufficient activation of the two inert reactants during urea synthesis.

3.2. Catalytic performance of MoP for urea production

After determining the unique geometrical structure and electronic properties of the Mo-terminated MoP-(101) surface, we further explored its catalytic performance for urea synthesis. Noteworthy, as summarized in Fig. 2, the cooperative reduction of N₂ and CO₂ in H₂O to produce urea ($\text{N}_2 + \text{CO}_2 + 6\text{H}^+ \rightarrow \text{CO}(\text{NH}_2)_2 + \text{H}_2\text{O}$) generally involves three key stages: (1) co-activation of N₂ and CO₂ molecules; (2) C–N coupling reaction; (3) hydrogenation of reaction intermediates, among which the first stage is a prerequisite during urea synthesis.

With these three key stages in mind, we first examined the adsorption of N₂ and CO₂ molecules on a MoP-(101) slab with Mo-termination to check if the first stage of urea production can proceed well. After considering various possible adsorption configurations (end-on and side-on configurations), we found that the N₂ molecule prefers to be adsorbed on the bridge sites of two Mo atoms *via* the side-on pattern, forming two Mo–N bonds with the lengths of 1.98 Å (Fig. 3a). Furthermore, the computed adsorption energy of N₂ (ΔE_{N_2}) is –1.05 eV, and the corresponding ΔG value is –0.43 eV, suggesting a spontaneous chemisorption process. Due to this strong interaction, the N–N bond length is elongated from 1.10 Å of the free N₂ molecule to 1.20 Å of the adsorbed N₂. After N₂ is strongly adsorbed, the chemisorption of CO₂ on its adjacent bridge site is also favorable, with the computed ΔE_{CO_2} of –1.09 eV (ΔG is –0.37 eV). In this configuration, both C and O atoms of *CO₂ bind with Mo active sites, forming Mo–O and Mo–C bonds with the lengths of 2.18 and 2.08 Å, respectively (Fig. 3b). As a result, the O–C–O bond angle is significantly bent (at about 47°) as compared with

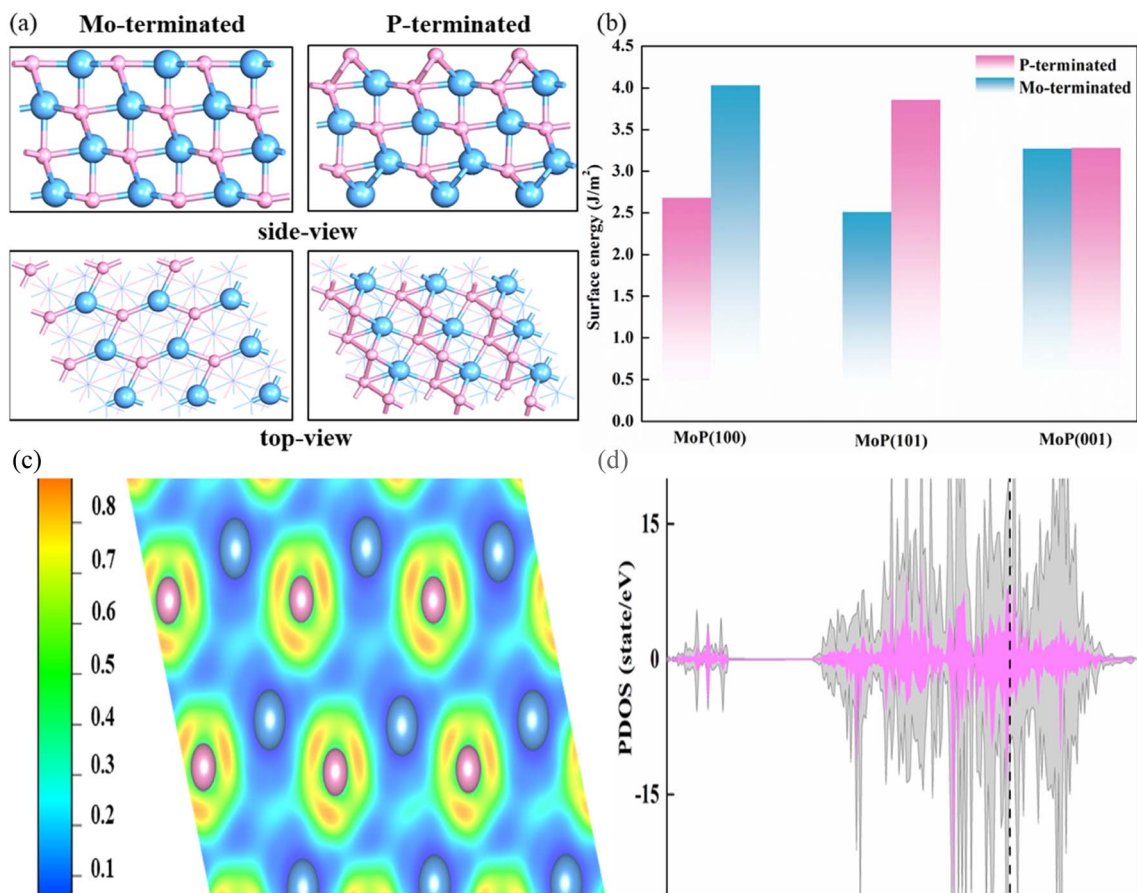


Fig. 1 (a) The optimized geometric structures of Mo-terminated (101) surface in MoP, (b) the surface energies (γ) of all the considered low-index surfaces of MoP with either Mo or P-terminations. The aquamarine blue and pink balls represent Mo and P atoms, respectively. (c) The computed electron localization function (ELF) and (d) projected density of states (PDOSs) of Mo-terminated MoP-(101) surface.

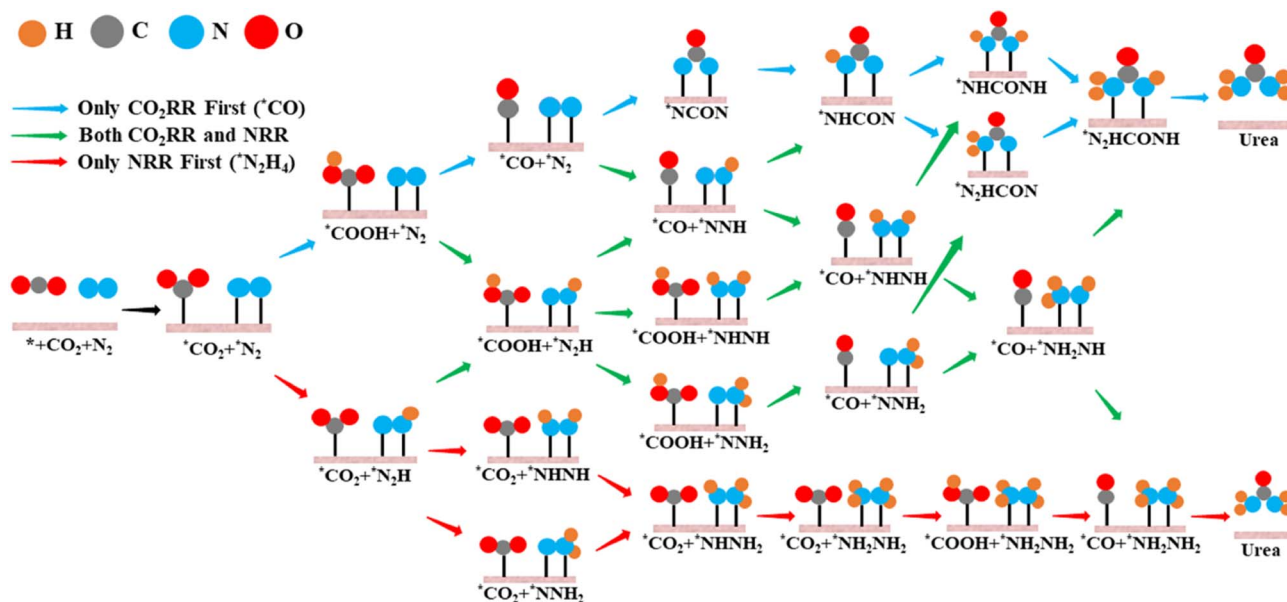


Fig. 2 Schematic depiction of all possible pathways for urea electrosynthesis.

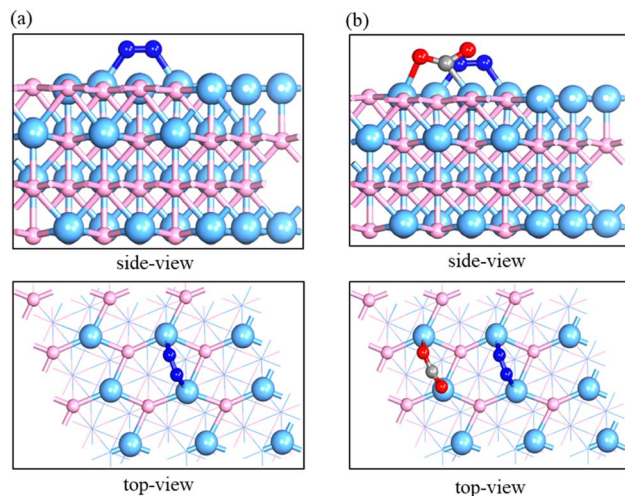


Fig. 3 The optimized geometrical structures for (a) N_2 and (b) $\text{N}_2 + \text{CO}_2$ adsorption on MoP-(101) surface. The aquamarine, pink, blue, gray, and red balls represent Mo, P, N, C, and O atoms, respectively.

the isolated linear CO_2 molecule. In addition, the presence of H protons can hinder the adsorption of adsorbent on the catalyst; thus, we also examined the adsorption energy of H^+ species on the MoP-(101) surface. Our results showed that the H^+ species will be adsorbed on the Mo sites, leading to the formation of three new Mo–H bonds with the adsorption energy of -0.81 eV, which is much lower than that of the adsorbed N_2 (-1.05 eV) and CO_2 (-1.09 eV), suggesting a more favorable adsorption of CO_2 and N_2 on the active sites. The aforementioned results undoubtedly suggested that both N_2 and CO_2 can be strongly chemisorbed and sufficiently activated on the MoP-(101) surface, which can be further verified by the strong hybridization with each other in the computed PDOSs (Fig. S3a†). Furthermore, the MoP-(101) surface transfers significant electrons to the adsorbed N_2 ($0.71|e|$) and CO_2 ($0.82|e|$) molecules

due to the “acceptance–donation” process, in which the MoP-(101) surface has empty d orbitals that can accept the lone-pair electrons of CO_2 and N_2 , and simultaneously donate electrons into the anti-bonding orbitals of CO_2 and N_2 . Interestingly, accumulating negative charges (Fig. S3b†) on the adsorbates facilitate their further hydrogenation by interacting with the positively charged H^+ species.

After confirming that N_2 and CO_2 molecules can be well activated upon co-adsorption on Mo-terminated MoP-(101) surface, we explored the feasibility of the C–N coupling reaction. Our computational results showed that the direct coupling between the adsorbed *N_2 and *CO_2 molecules on MoP-(101) slab is not possible, as they will be spontaneously separated after full atomic relaxation (Fig. S4†). To this end, we further explored the hydrogenation of the adsorbed N_2 and CO_2 species. Interestingly, after one proton-coupled electron transfer (PCET) step, the O atom of *CO_2 prefers to be hydrogenated to *COOH with a ΔG of -0.51 eV, which is much lower than that of $\text{*N}_2\text{H}$ formation ($\Delta G = -0.06$ eV). Subsequently, the approach of a second ($\text{H}^+ + \text{e}^-$) to *COOH generates the key *CO intermediate by releasing a H_2O molecule. Remarkably, this elementary step ($\text{*N}_2 + \text{*COOH} + \text{H}^+ + \text{e}^- \rightarrow \text{*N}_2 + \text{*CO} + \text{H}_2\text{O}$) is uphill by only 0.17 eV in the free energy profile, which is slightly lower than that of the formation of ($\text{*N}_2\text{H} + \text{*COOH}$, 0.21 eV). These computational results suggested that the formation of intermediate species *N_2 and *CO is more energetically favorable than that of other species on the MoP-(101) surface.

Next, we explored the possibility of *NCON formation by the C–N coupling reaction on this MoP surface, inspired by the recent pioneering work of Li's group:^{20,43} the coupling between *CO and *N_2 to generate a tower-like *NCON intermediate is a pivotal step in urea synthesis. As shown in Fig. S5,† we found that the reaction of $\text{*N}_2 + \text{*CO} \rightarrow \text{*NCON}$ is endothermic by 0.48 eV, and the involved energy barrier (1.87 eV) is also much higher than those of the reported Pd–Cu catalyst (0.79 eV),²⁰ MBene materials (0.42 – 1.00 eV),^{43,44} and double-atom catalysts

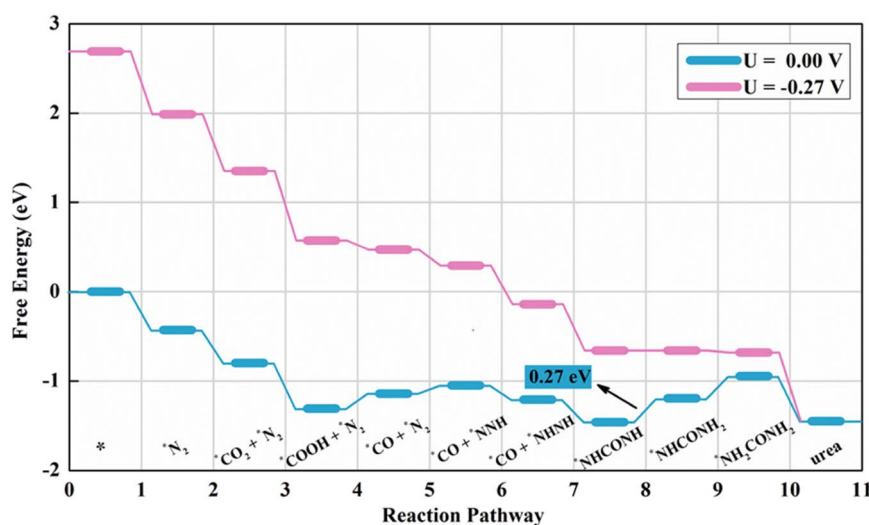


Fig. 4 The computed free energy profiles for urea electrosynthesis on Mo-terminated MoP-(101) surface at zero and applied potentials. The structures of the involved reaction intermediates are presented in Fig. S8.†

(1.18–1.62 eV) anchored on N-doped graphene.⁴⁵ Thus, we predicted that the formation of $^*\text{NCON}$ through the coupling between the adsorbed $^*\text{N}_2$ and $^*\text{CO}$ species on MoP catalyst is unfavorable both thermodynamically and kinetically.

Since the adsorbed $^*\text{N}_2$ and $^*\text{CO}$ intermediates cannot couple with each other to generate $^*\text{NCON}$ species, we examined their further hydrogenation to give ($^*\text{N}_2\text{H} + ^*\text{CO}$), ($^*\text{N}_2 + ^*\text{COH}$), or ($^*\text{N}_2 + ^*\text{HCO}$). The computational results showed that the formation of ($^*\text{N}_2\text{H} + ^*\text{CO}$) is energetically more favorable; its ΔG value (0.09 eV) is much lower than the other two hydrogenation steps (1.34 and 0.91 eV, respectively, see Table S1†). In addition, to further demonstrate that N_2 is preferentially hydrogenated, the kinetic process of the first step of hydrogenation was also considered. Our results showed that the barrier energy to form $^*\text{N}_2\text{H} + ^*\text{CO}$, $^*\text{N}_2 + ^*\text{COH}$, and $^*\text{N}_2 + ^*\text{HCO}$ is 1.07, 2.38 and 1.58 eV, respectively, suggesting that the formed $^*\text{N}_2\text{H} + ^*\text{CO}$ is kinetically most favorable (Fig. S6†). Subsequently, the formed ($^*\text{N}_2\text{H} + ^*\text{CO}$) is readily hydrogenated to ($^*\text{N}_2\text{H}_2 + ^*\text{CO}$) due to its lower ΔG value (−0.16 eV) than those of other competitive steps, including formation of HNCON (−0.06 eV), $^*\text{N}_2\text{H} + ^*\text{CHO}$ (0.94 eV), and $^*\text{N}_2\text{H} + ^*\text{COH}$ (1.41 eV). For the ($^*\text{N}_2\text{H}_2 + ^*\text{CO}$) intermediate, the $^*\text{CO}$ can be inserted into the N–N bond, leading to the formation of $^*\text{NHCOHN}^*$. Notably, in this structure, the N–N bond is broken with a distance of 2.37 Å, accompanied with the formation of two C–N bonds with the lengths of 1.39 Å. Especially, from the thermodynamic perspective, the formation of $^*\text{NHCOHN}^*$ is exothermic, and the ΔG value is −0.25 eV. In contrast, the hydrogenation of ($^*\text{N}_2\text{H}_2 + ^*\text{CO}$) is endothermic by 0.16 eV to ($^*\text{N}_2\text{H}_3 + ^*\text{CO}$), 0.98 eV to ($^*\text{N}_2\text{H}_2 + ^*\text{CHO}$), and 1.45 eV to ($^*\text{N}_2\text{H}_2 + ^*\text{COH}$). Kinetically, the computed energy barrier of this coupling process is 1.30 eV (Fig. S7†), which is comparable to those of previously reported catalysts (0.58–1.62 eV)^{20,43,45} and is even lower than the thermodynamics overpotential value of 1.67 eV.⁴⁶ Thus, the C–N coupling of $^*\text{N}_2\text{H}_2$ and $^*\text{CO}$ on the MoP-(101) surface is thermodynamically and kinetically feasible, playing a critical role for efficient urea production.

After the generation of the key $^*\text{NHCOHN}^*$ intermediate through C–N coupling, its further hydrogenation on Mo-(101) slab was explored. It was found that $^*\text{NHCONH}$ is reduced to the urea product *via* two PCET steps with ΔG values of 0.27 and 0.25 eV, respectively. Finally, the formed urea is easily released from the MoP-(101) surface, as urea has a quite small adsorption energy (−0.28 eV) on this catalyst, much lower than that of the Pd–Cu catalysts (−1.68 eV).²⁰

Overall, the most favorable pathway for urea production from the cooperative reduction of N_2 and CO_2 on Mo-terminated MoP-(101) surface can be summarized as: $\text{N}_2 + \text{CO}_2 \rightarrow ^*\text{N}_2 + ^*\text{CO}_2 \rightarrow ^*\text{N}_2 + ^*\text{CO}_2 \rightarrow ^*\text{N}_2 + ^*\text{COOH} \rightarrow ^*\text{N}_2 + ^*\text{CO} \rightarrow ^*\text{N}_2\text{H} + ^*\text{CO} \rightarrow ^*\text{N}_2\text{H}_2 + ^*\text{CO} \rightarrow ^*\text{NHCONH}^* \rightarrow ^*\text{NHCONH}_2^* \rightarrow ^*\text{NH}_2\text{CONH}_2 \rightarrow \text{NH}_2\text{CONH}_2$ (Fig. 4 and S8†). Since the formation of $^*\text{NHCONH}_2^*$ exhibits the largest ΔG value (0.27 eV) among all the elementary steps, this step is the potential-limiting step, and the corresponding limiting potential for urea production (U_L^{urea}) is −0.27 V, which is much less negative than that of the state-of-the-art Pd–Cu catalyst in experiments and those of other theoretically designed electrocatalysts (−0.49 to −0.79 V),^{20,45} indicating the superior

electrocatalytic activity of MoP toward urea formation. Furthermore, to simulate a real aqueous solution, we computed the free energy to generate urea by using an explicit solvent model (Fig. S9†). Our results showed that the potential limiting step changes from formation of $^*\text{NHCONH}_2$ (vacuum) to the formation of $^*\text{N}_2 + ^*\text{COOH}$ (water), with a small change in the limiting potential. Notably, we also computed the Gibbs free energy of the MoP-(001) and MoP-(100) surface. Our results showed that the limiting potential of MoP-(001) and MoP-(100) is 1.34 and 0.73 eV, respectively; these values are larger than those of the MoP-(101) surface, and thus the MoP-(101) surface has the highest urea activity (Fig. S10†).

3.3. Reaction selectivity toward urea synthesis

During the process of urea electrosynthesis, NRR is the main competitive reaction, which may significantly lower the faradaic efficiency. According to previous studies,²⁷ Mo-based materials usually exhibit high activity for NRR. On the MoP-(101) surface, we found that the N_2 reduction to NH_3 prefers to follow the alternative mechanism; the computed U_L^{NRR} value (−0.86 V, Fig. S11†) is three times more negative than that of U_L^{urea} (−0.27 V). According to the aforementioned results, we expect the formation of urea on MoP.

3.4. Proof-of-concept experiment

In order to confirm our above theoretical predictions, we used commercial MoP nanoparticles to evaluate their electrocatalytic performance for urea synthesis. The X-ray diffraction (XRD) pattern of the sample (Fig. 5a) can be indexed to the standard MoP phase. The peaks at 27.9°, 32.0°, 43.0°, 57.1°, 57.7°, 64.8°, 67.0°, 67.5°, and 74.1° correspond to the (001), (100), (101), (110), (002), (111), (200), (102) and (201) planes of MoP phase, respectively.⁴⁷ The scanning electron microscopy (SEM) image (Fig. 5b) shows that the particle size of the commercial MoP nanoparticles is about 3 μm. The relevant elemental mapping (Fig. S12†) indicates Mo and P are evenly distributed, and the atomic ratio of these two elements is about 1:1 (Fig. S12†). Moreover, the high-resolution transmission electron microscopy (HRTEM) image (Fig. 5c) shows that MoP nanoparticles have high crystallinity with the lattice spacing of 0.279 nm and 0.210 nm, corresponding to the (101) and (100) crystal planes of MoP, respectively.^{48,49} To further determine the surface atomic states of Mo and P in the samples, we performed X-ray photoelectron spectroscopy (XPS). In the Mo 3d spectrum (Fig. 5d), the peaks at 228.3 eV and 232 eV can be attributed to Mo–P bonds, while the peaks at 233.1 eV and 235.8 eV are attributed to Mo^{6+} ; the peaks at 232.5 eV and 228.7 eV are assigned to Mo^{4+} , which are due to the surface oxidation of the sample in air. In the P 2p spectrum (Fig. S13b†), the peaks at 129.7 eV and 130.6 eV are assigned to the bonding between P and Mo, while the peak at 134.2 eV represents the P–O bond, which is a typical peak for the surface oxidation of metal phosphides in air.⁵⁰

Then, we measured the prepared catalyst's performance for the electrochemical synthesis of urea in an H-type two-chamber electrolytic cell with 0.1 M KHCO_3 solution. Ultrahigh-purity CO_2 (99.999%) and N_2 (99.999%) gas mixture was

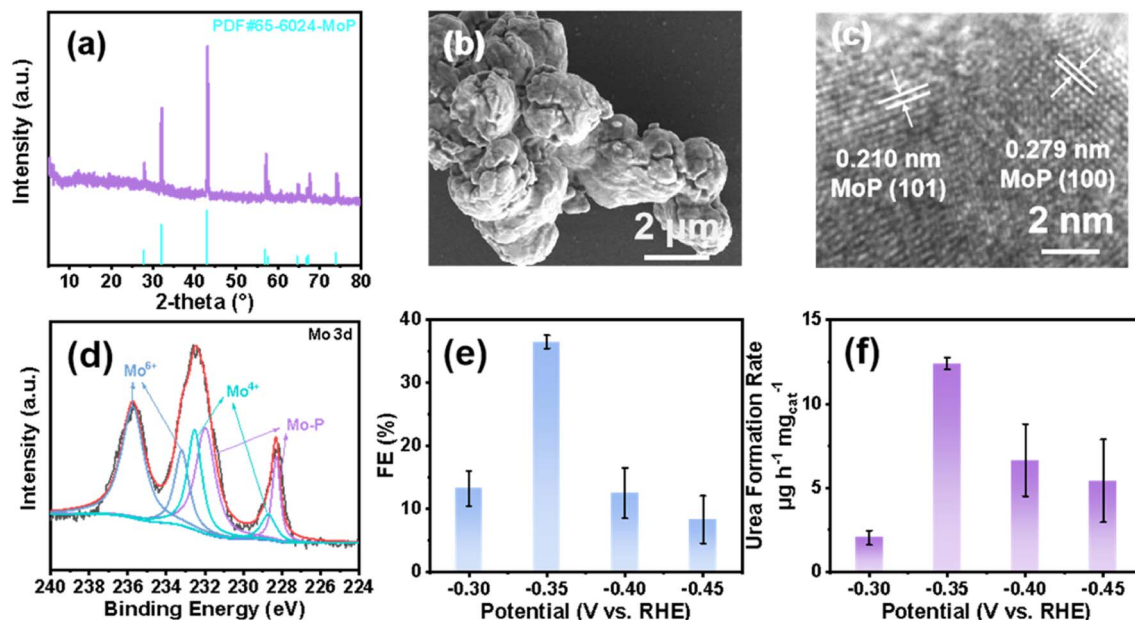


Fig. 5 (a) XRD pattern of MoP nanoparticles. (b) SEM image MoP nanoparticles. (c) HRTEM image of MoP nanoparticles. (d) XPS spectra of Mo 3d of MoP nanoparticles. (e) Faradaic efficiencies of urea at different working potentials for MoP. (f) Urea formation rates at different working potentials for MoP ($\mu\text{g h}^{-1} \text{mg}^{-1}$).

continuously fed into the cathode chamber during the reaction. The liquid product (urea) formed in the electrolyte was determined by the diacetyl monoxime method. The calibration curve is displayed in Fig. S14†. Constant potential electrolysis tests were used to quantitatively evaluate the ability for urea synthesis at different working potentials; the samples were kept for two hours at each potential (Fig. S15†). The experimental results illustrate that the highest faradaic efficiency of 36.5% (Fig. 5e) and the highest urea formation rate of $12.4 \mu\text{g h}^{-1} \text{mg}_{\text{cat}}^{-1}$ (Fig. 5f) both occur at -0.35 V . Particularly, the achieved FE and yield rate for urea production on MoP nanoparticles are comparable to previously reported catalysts (Table S2†),^{20,22,46} suggesting their good catalytic performance for urea generation. In addition, we also tested the MoP samples from different producers. Our results showed that the FE and yield of urea are generally comparable, further suggesting that MoP can be an effective electrocatalyst for urea synthesis (Fig. S16†).

Furthermore, to prove that the urea is generated during the simultaneous reduction of N_2 and CO_2 by MoP as a catalyst, we conducted potentiostatic tests under different conditions. We barely detected urea either using Ar as feed gas or pouring the mixed gas (N_2 and CO_2) into the electrolyte tank under the condition of open circuit potential. Besides, if we only pump N_2 or CO_2 into the electrolytic cell, it was challenging to discover urea in the electrolyte after the reaction (Fig. S17†). These results prove that urea was generated from the reduction of CO_2 and N_2 using MoP as the catalyst. In order to illustrate that MoP is the active substance for catalyzing urea synthesis, we used different electrodes for electrochemical tests, like carbon paper with nothing loaded and MoO_2 or MoO_3 loaded on carbon paper, under the same conditions; all three electrodes produced much less urea than MoP loaded on carbon paper (Fig. S18–

S20†). This indicates that MoP is the catalytically active substance, rather than MoO_x or carbon paper. To further explore the stability of the catalyst, we carried out XRD tests on the electrode after reaction. In the XRD pattern (Fig. S21†), it can be observed that the characteristic peaks of MoP after reaction still exist and no other peak appears, which indicates that the MoP was not reduced during the electrochemical reaction. Besides that, the SEM image of MoP after the reaction (Fig. S22†) also proves that the MoP has no significant change in morphology during the reaction. Further, we tested the cyclic stability of MoP, and it can be seen that after five consecutive cycles (Fig. S23†), there was only a slight decrease in FE, but the urea formation rate dropped by nearly 30%, probably because the catalyst fell off the carbon paper during the reaction. In addition, we tested the XRD after reactions at different potentials. Our results showed that the lattice of MoP-(101) facets at different potentials has no significant change (Fig. S24†). These prove that the stability of the catalyst is relatively good. To further determine whether the adsorption of N_2 and CO_2 is stable at the operating voltage (for details, see Fig. S25†), we computed N_2 and CO_2 co-adsorption energy on the MoP-(101) surface at -0.35 V , under which the highest faradaic efficiency and the highest urea formation rate were obtained experimentally. Our results showed that the co-adsorption energy of ($^*\text{N}_2 + ^*\text{CO}_2$) on MoP-(101) is -1.15 eV , indicating that the co-adsorption of N_2 and CO_2 is stable at operating voltages.

4. Conclusion

In summary, by means of DFT computations, we explored the potential of MoP as a promising electrocatalyst for urea synthesis. Our results revealed that the exposed Mo active sites

in the MoP-(101) surface exhibit high reactivity towards the simultaneous activation of N_2 and CO_2 . Through a key *NHCOHN* intermediate, the adsorbed N_2 and CO_2 can be effectively converted to urea with an ultralow limiting potential (-0.27 V vs. RHE), accompanied by excellent selectivity due to the great suppression effects on competitive NRR. Such theoretical computations were then experimentally verified using the MoP nanoparticles, which exhibit good performance for urea synthesis, with urea yield rate of $12.4 \mu\text{g h}^{-1} \text{mg}^{-1}$ and faradaic efficiency of 36.5% at -0.35 V vs. RHE, suggesting the high activity and excellent selectivity of MoP for urea electro-synthesis. This work sheds light on the critical role of abundant Mo active sites for simultaneously converting inert N_2 and CO_2 into urea at ambient conditions, which will inspire more studies to further develop advanced electrocatalysts and to comprehensively reveal the underlying mechanisms for this challenging and complicated, but highly rewarding, reaction.

Conflicts of interest

The authors declare no competing financial interest.

Acknowledgements

This work was financially supported in China by the Natural Science Funds for Distinguished Young Scholar of Heilongjiang Province (No. JC2018004) and Natural Science Foundation of Heilongjiang Province of China (TD2020B001), and the in USA by the NSF-CREST Center for Innovation, Research and Education in Environmental Nanotechnology (CIRE2N, Grant Number HRD-1736093) and the STARS Award (2021) of the University of Texas System. This work was also supported by the National Natural Science Foundation of China (No. 12034002, 51872116, and 22279044), the Jilin Province Science and Technology Development Program (20210301009GX). The authors also acknowledge the computational resource supported by Harbin Normal University.

References

- 1 J. W. Erisman, M. A. Sutton, J. Galloway, Z. Klimont and W. Winiwarter, *Nat. Geosci.*, 2008, **1**, 636–639.
- 2 B. M. Comer, P. Fuentes, C. O. Dimkpa, Y.-H. Liu, C. A. Fernandez, P. Arora, M. Realff, U. Singh, M. C. Hatzell and A. J. Medford, *Joule*, 2019, **3**, 1578–1605.
- 3 X. Zhang, E. A. Davidson, D. L. Mauzerall, T. D. Searchinger, P. Dumas and Y. Shen, *Nature*, 2015, **528**, 51–59.
- 4 Y. Liu, X. Zhao and L. Ye, *Ind. Eng. Chem. Res.*, 2016, **55**, 8743–8750.
- 5 L. Celleno, *Dermatol. Ther.*, 2018, **31**, e12690.
- 6 W. Xu, Z. Wu and S. Tao, *Energy Technol.*, 2016, **4**, 1329–1337.
- 7 E. T. Sayed, T. Eisa, H. O. Mohamed, M. A. Abdelkareem, A. Allagui, H. Alawadhi and K.-J. Chae, *J. Power Sources*, 2019, **417**, 159–175.
- 8 D. B. Kayan and F. Köleli, *Appl. Catal., B*, 2016, **181**, 88–93.
- 9 M. Yuan, J. Chen, Y. Bai, Z. Liu, J. Zhang, T. Zhao, Q. Shi, S. Li, X. Wang and G. Zhang, *Chem. Sci.*, 2021, **12**, 6048–6058.
- 10 S. Licht, B. Cui, B. Wang, F.-F. Li, J. Lau and S. Liu, *Science*, 2014, **345**, 637–640.
- 11 J. Qian, Q. An, A. Fortunelli, R. J. Nielsen and W. A. Goddard, *J. Am. Chem. Soc.*, 2018, **140**, 6288–6297.
- 12 G. Chen Jingguang, M. Crooks Richard, C. Seefeldt Lance, L. Bren Kara, R. M. Bullock, Y. Darensbourg Marcetta, L. Holland Patrick, B. Hoffman, J. Janik Michael, K. Jones Anne, G. Kanatzidis Mercouri, P. King, M. Lancaster Kyle, V. Lymar Sergei, P. Pfromm, F. Schneider William and R. Schrock Richard, *Science*, 2018, **360**, eaar6611.
- 13 S. Giddey, S. P. S. Badwal and A. Kulkarni, *Int. J. Hydrogen Energy*, 2013, **38**, 14576–14594.
- 14 H. Liu, *Chin. J. Catal.*, 2014, **35**, 1619–1640.
- 15 J. Baltrusaitis, *ACS Sustainable Chem. Eng.*, 2017, **5**, 9527.
- 16 C. Lv, L. Zhong, H. Liu, Z. Fang, C. Yan, M. Chen, Y. Kong, C. Lee, D. Liu, S. Li, J. Liu, L. Song, G. Chen, Q. Yan and G. Yu, *Nat. Sustain.*, 2021, **4**, 868–876.
- 17 G. Soloveichik, *Nat. Catal.*, 2019, **2**, 377–380.
- 18 C. Chen, N. He and S. Wang, *Small Sci.*, 2021, **1**, 2100070.
- 19 M. Yuan, H. Zhang, Y. Xu, R. Liu, R. Wang, T. Zhao, J. Zhang, Z. Liu, H. He, C. Yang, S. Zhang and G. Zhang, *Chem Catal.*, 2022, **2**, 309–320.
- 20 C. Chen, X. Zhu, X. Wen, Y. Zhou, L. Zhou, H. Li, L. Tao, Q. Li, S. Du, T. Liu, D. Yan, C. Xie, Y. Zou, Y. Wang, R. Chen, J. Huo, Y. Li, J. Cheng, H. Su, X. Zhao, W. Cheng, Q. Liu, H. Lin, J. Luo, J. Chen, M. Dong, K. Cheng, C. Li and S. Wang, *Nat. Chem.*, 2020, **12**, 717–724.
- 21 M. Yuan, J. Chen, Y. Xu, R. Liu, T. Zhao, J. Zhang, Z. Ren, Z. Liu, C. Streb, H. He, C. Yang, S. Zhang and G. Zhang, *Energy Environ. Sci.*, 2021, **14**, 6605–6615.
- 22 M. Yuan, J. Chen, Y. Bai, Z. Liu, J. Zhang, T. Zhao, Q. Wang, S. Li, H. He and G. Zhang, *Angew. Chem., Int. Ed.*, 2021, **60**, 10910–10918.
- 23 V. S. Saji and C.-W. Lee, *ChemSusChem*, 2012, **5**, 1146–1161.
- 24 Y. Li, Z. Yin, X. Liu, M. Cui, S. Chen and T. Ma, *Mater. Today Chem.*, 2021, **19**, 100411.
- 25 Y. Jiang, Y. Wang, J. Ni and L. Li, *InfoMat*, 2021, **3**, 339–352.
- 26 W. Hua, H.-H. Sun, F. Xu and J.-G. Wang, *Rare Met.*, 2020, **39**, 335–351.
- 27 X. Guo, X. Wan and J. Shui, *Cell Rep. Phys. Sci.*, 2021, **2**, 100447.
- 28 H. Y. Zhou, Y. B. Qu, J. C. Li, Z. L. Wang, C. C. Yang and Q. Jiang, *Appl. Catal., B*, 2022, **305**, 121023.
- 29 W. Wu, C. Niu, P. Yan, F. Shi, C. Ma, X. Yang, Y. Jia, J. Chen, M. I. Ahmed, C. Zhao and Q. Xu, *Appl. Catal., B*, 2021, **298**, 120615.
- 30 X. Sun, L. Lu, Q. Zhu, C. Wu, D. Yang, C. Chen and B. Han, *Angew. Chem., Int. Ed.*, 2018, **57**, 2427–2431.
- 31 P. Xiao, M. A. Sk, L. Thia, X. Ge, R. J. Lim, J.-Y. Wang, K. H. Lim and X. Wang, *Energy Environ. Sci.*, 2014, **7**, 2624–2629.
- 32 Z. Xing, Q. Liu, A. M. Asiri and X. Sun, *Adv. Mater.*, 2014, **26**, 5702–5707.
- 33 P. Liu and J. A. Rodriguez, *Catal. Lett.*, 2003, **91**, 247–252.
- 34 G. Kresse and J. Hafner, *Phys. Rev. B: Condens. Matter Mater. Phys.*, 1993, **47**, 558–561.

- 35 G. Kresse and J. Furthmüller, *Phys. Rev. B: Condens. Matter Mater. Phys.*, 1996, **54**, 11169–11186.
- 36 P. E. Blöchl, *Phys. Rev. B: Condens. Matter Mater. Phys.*, 1994, **50**, 17953–17979.
- 37 G. Kresse and D. Joubert, *Phys. Rev. B: Condens. Matter Mater. Phys.*, 1999, **59**, 1758–1775.
- 38 J. P. Perdew, K. Burke and M. Ernzerhof, *Phys. Rev. Lett.*, 1996, **77**, 3865–3868.
- 39 S. Grimme, *J. Comput. Chem.*, 2006, **27**, 1787–1799.
- 40 G. Henkelman, B. P. Uberuaga and H. Jónsson, *J. Chem. Phys.*, 2000, **113**, 9901–9904.
- 41 J. K. Nørskov, J. Rossmeisl, A. Logadottir, L. Lindqvist, J. R. Kitchin, T. Bligaard and H. Jónsson, *J. Phys. Chem. B*, 2004, **108**, 17886–17892.
- 42 A. A. Peterson, F. Abild-Pedersen, F. Studt, J. Rossmeisl and J. K. Nørskov, *Energy Environ. Sci.*, 2010, **3**, 1311–1315.
- 43 X. Zhu, X. Zhou, Y. Jing and Y. Li, *Nat. Commun.*, 2021, **12**, 4080.
- 44 Y. Xiao, C. Shen, Z. Xiong, J. Li and W. Zhang, *Mater. Today Phys.*, 2022, **26**, 100726.
- 45 C. Zhu, M. Wang, C. Wen, M. Zhang, Y. Geng, G. Zhu and Z. Su, *Adv. Sci.*, 2022, **9**, 2105697.
- 46 J. Mukherjee, S. Paul, A. Adalder, S. Kapse, R. Thapa, S. Mandal, B. Ghorai, S. Sarkar and U. K. Ghorai, *Adv. Funct. Mater.*, 2022, **32**, 2200882.
- 47 D. Wang, Y. Shen, X. Zhang and Z. Wu, *J. Mater. Sci.*, 2017, **52**, 3337–3343.
- 48 B. Liu, H. Li, B. Cao, J. Jiang, R. Gao and J. Zhang, *Adv. Funct. Mater.*, 2018, **28**, 1801527.
- 49 Z. Pu, I. S. Amiinu, X. Liu, M. Wang and S. Mu, *Nanoscale*, 2016, **8**, 17256–17261.
- 50 L. Chai, W. Yuan, X. Cui, H. Jiang, J. Tang and X. Guo, *RSC Adv.*, 2018, **8**, 26871–26879.